ACS OMEGA

http://pubs.acs.org/journal/acsodf

Article

Design and Performance of an Acoustic Levitator System Coupled with a Tunable Monochromatic Light Source and a Raman Spectrometer for *In Situ* Reaction Monitoring

Beni B. Dangi* and Daniel J. Dickerson

Cite This: *ACS Omega* 2021, 6, 10447−10453

Read Online

ACCESS | Metrics & More | Article Recommendations

ABSTRACT: The design and performance of a custom-built reaction chamber combined with an acoustic levitator, a tunable monochromatic light source, and a Raman spectrometer are reported. The pressure-compatible reaction chamber was vacuum-tested and coupled with the acoustic levitator that allows contactless sample handling, free of contingent sample requirements such as charge and refractive index. The calibration and performance of the Raman spectrometer was studied utilizing gated detection and three different gratings that can be interchanged within seconds for a desired resolution and photon collection range. A wide range of 186−5000 cm^{-1} Raman shift, with a small uncertainty of ±2 cm^{-1}, can be recorded covering a complete vibrational range in chemical reaction monitoring. The gating of the detector allowed operation under the room light and filtration of unwanted sample fluorescence. The *in situ* reaction perturbation and monitoring of physical and chemical changes of samples by the Raman system were demonstrated by degradation of polystyrene by monochromatic UV light and photobleaching of a potato slice by visible light. This instrument provides a versatile platform for *in situ* investigation of surface reactions, without external support structures and under controlled pressure and radiation conditions, relevant to various disciplines such as materials science, astrochemistry, and molecular biology.

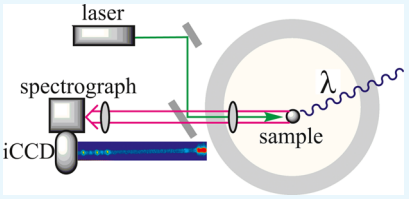

1. INTRODUCTION

In recent years, acoustic levitation[1−4] has been utilized in a range of scientific disciplines including but not limited to analytical chemistry, astrochemistry, materials science, and pharmaceuticals.[2,5−8] Acoustic levitation has also been used in contactless mixing of two droplets to initiate a chemical reaction[9,10] and to transport protein crystal samples in crystallography experiments.[11] In acoustic levitation, a liquid droplet, a solid particle, or a suspension is levitated slightly below the pressure nodes of the ultrasonic standing wave. The major advantages of such a levitation technique lie in the removal of often complicating effects of a contacting surface on the sample. The absence of a contacting surface or a wall also increases the sensitivity of the spectroscopic detection techniques such as infrared spectroscopy, Raman spectroscopy, mass spectrometry, and X-ray diffraction utilized to study the chemical and physical modifications of the levitated droplet/particle. Furthermore, a levitator can be used to probe the differences between the physical and chemical processes on the bulk samples and the surfaces of sub-millimeter size levitated particles.[5,12] Such tiny particles floating in the given gas medium provide ideal laboratory conditions simulating the dust particles or droplets in the atmospheres of planets and exoplanets.[5] Moreover, the levitated particle can respond quickly to temperature and radiation perturbations due to their small total heat and radiation dose capacity. Hence, a levitation device provides a versatile platform to study the physical and chemical processes without support structures as well as creates less-contingent sample trapping requirements, such as electric charge and refractive index.

In combination with a controlled gas and radiation environment, acoustic levitation provides a strong and relatively unexplored avenue for studying how a sample might behave in a variety of atmospheric conditions. For example, acoustic levitation has been gaining traction in the space science community for its potential in low-gravity simulation experiments.[13,14] The ability to suspend micrometer-sized particles or droplets in a given gas medium provides ideal laboratory conditions for simulating interplanetary dust particles and micrometeoroids that can be found in the atmospheres of planets and exoplanets. In such laboratory experiments, gas−surface, heterogeneous reactions are of particular interest to investigate cloud and haze dynamics.[5,15] In a gas−surface reaction investigation, reactions of unsaturated hydrocarbon gases on the surface of silicon single particle had been performed,[4] where selected hydrocarbon gases are adsorbed on the surface and polymerized to refractory

Received: February 19, 2021
Accepted: March 29, 2021
Published: April 9, 2021

ACS Publications

© 2021 The Authors. Published by American Chemical Society

https://doi.org/10.1021/acsomega.1c00921
ACS Omega 2021, 6, 10447−10453

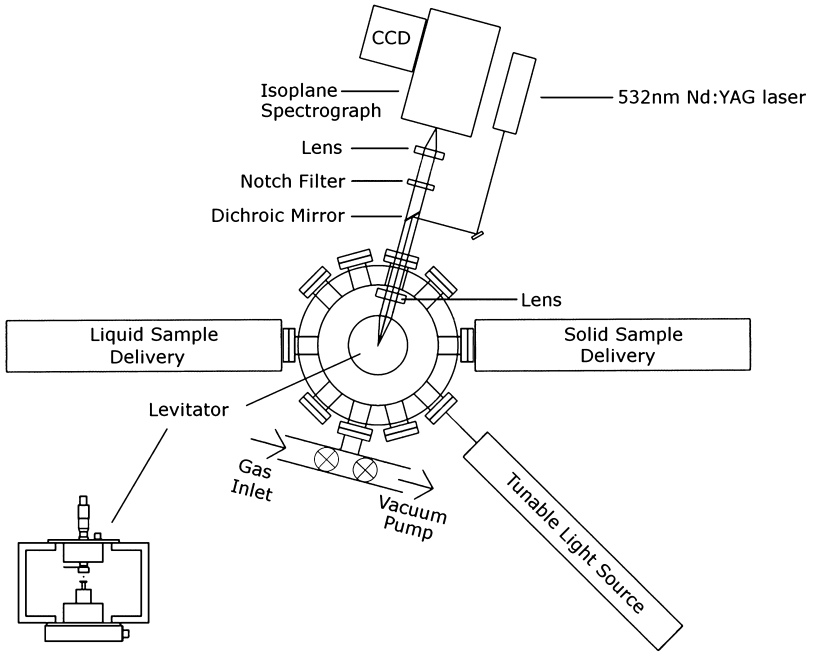

Figure 1. Top view of the schematic of the instrumental setup. The side view of the levitator is shown for clarity. The sample delivery system, tunable light source, and Raman spectroscopic detection are coupled with the main process chamber. The schematic sketch is not drawn to the scale.

carbonaceous compounds whose spectroscopic signatures matched with the meteoritic sample providing insights into the possible formation conditions of the carbonaceous compounds in the meteoritic sample. A model mechanistic computational study[16] showed that 1,3-butadiene ($H_2CHCHCH_2$) can adsorb exothermically on the silicon surface propagated by a second $H_2CHCHCH_2$ molecule adsorption with further release of energy. Free radical formation and further chain propagation likely lead to the removal of hydrogen atoms with increasing carbon content to form the complex product mixture. This finding might explain the lower than expected methane to carbon monoxide (CH_4/CO) ratio in the hot Neptune GJ 436b, where the abundant methane photochemically converts to higher order hydrocarbons and ultimately to refractory graphitic carbon in the presence of catalytic silicon surface. Furthermore, the liquid droplets are often used as a reaction medium for varieties of physical and chemical reaction processes, such as nucleation and crystallization in a container processing, but recently, such reactions have been the subject of investigation under levitation conditions.[17,18] However, the time scales of such reactions may be longer than the evaporation time of these small liquid droplets.[19,20] Hence, it is of prime interest to prolong the evaporation lifetime of liquid droplets. Recently, experiments have been performed on the evaporation times and trends of microliter volumes of common solvent methanol and water under normal container processing and under the acoustic levitation conditions. Results showed several fold increase on lifetime of the droplet in the later conditions.[21] Evaporations of solutions resulted in recovery of the solute material but with trapped solvent inside the residue under ambient conditions.

Even though the experiments described above approximately simulate the temperature and pressure conditions in selected exoplanet atmospheres, such as hot Jupiters and Neptunes,[22,23] and provide a glimpse of the initial reaction and products, systematic improvements in laboratory simulation conditions such as host star radiation in the atmospheres, as well as detection techniques, are highly desirable. By utilizing monochromatic light from UV to IR range, it is possible to obtain information on the wavelength-dependent reactions on the surface of levitated particles. Such experiments might also yield valuable information on the underlying, hitherto largely unknown, reaction mechanism. Here, we describe the design and performance of a pressure-compatible reaction chamber equipped with an acoustic levitator and a tunable monochromatic light source (240−2400 nm) as the radiation source and demonstrate its applicability in inducing the chemical and physical changes on polystyrene microparticles. Photobleaching of a sliced potato sample with visible light was demonstrated for the instrument's potential applications in chemical monitoring of agricultural products and environmental samples. To record the reaction changes *in situ*, a custom-built Raman spectroscopic system was interfaced with the reaction chamber and acoustic levitator. While the reaction chamber and levitator enclosure designs are similar to that reported by Brotton and Kaiser,[4] addition of the tunable light source and the three-grating Raman spectrometer system adds into the instrumental capability. While such capability is enhanced in our instrument, Brotton and Kaiser have additional probes of IR and UV−vis spectroscopies. Calibration, performance, and application in monitoring chemical signatures during sample physical and chemical transformation are described in detail. Such Raman spectral recordings over a time period also allow kinetic studies in formation, destruction, or transformation reactions on surfaces as well as identification of reactants and products based on their vibrational signatures.

2. RESULTS AND DISCUSSION

2.1. Reaction Chamber and Levitation Device. The design of the reaction chamber is similar to that reported by Brotton and Kaiser[4] with fewer access ports. The experimental

https://doi.org/10.1021/acsomega.1c00921
ACS Omega 2021, 6, 10447−10453

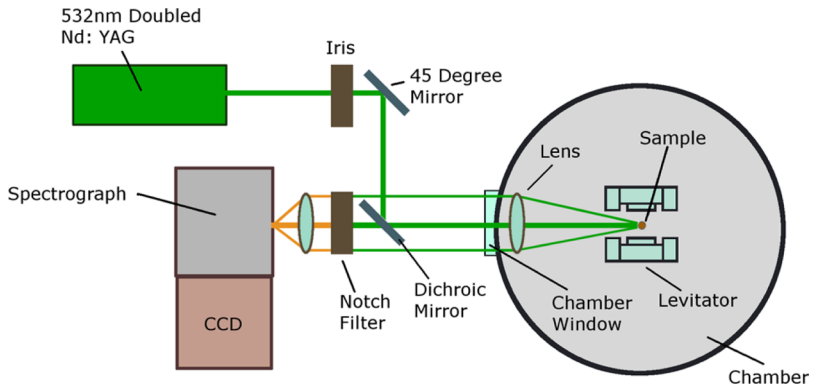

Figure 2. Schematic of the Raman spectroscopic system (not drawn to the scale). Details of parts and timing sequence are given in the text.

setup is depicted in the schematic diagram as shown in Figure 1. A stainless steel reaction chamber with 10 side ports (2.75 CF) and top and bottom ports (13.25 CF) with 22 L volume was custom-built by Kurt J. Lesker company. An acoustic levitator (Tec5USA, T-121378) was fixed at the center of the stainless steel reaction chamber using threaded screws via four posts that connect the transducer base with the reflector. The distance between the transducer and the reflector of the single-axis levitator can be adjusted with the micrometer adjuster attached at the top of the reflector to optimize the levitation node, which changes according to gas pressure and levitation power.[1] The levitator transducer was operated at a fixed frequency of 56 kHz and amplitude between 4 and 6 W with the reflector operated at typically 10 mm from the transducer to create nodes for sample suspension. An oscilloscope (Tektronix, TDS2012CC041875) was used to monitor the sound waves and resonance conditions throughout the experiment. A pin connector was utilized through a chamber port for power supply to the levitator.

A liquid droplet/suspension or a solid particle sample was delivered utilizing two separate ports, as shown in Figure 1. For the liquid, a small amount (typically 1−2 μL) of the sample was placed at the levitation nodes using a 22-gauge needle (Hamilton Company, KF722), which was connected using a 22-gauge Teflon tube (Hamilton Company, 86510). The tube is connected inside the chamber to an adapter, which was vacuum tight on a custom-built flange. The luer lock adapter (Hamilton Company, 86511) on the outside of the chamber was connected to another tubing which was connected to a 100 μL syringe (Hamilton Company, 1710TLL) with the sample. The solid sample delivery system uses another side port. A vacuum-compatible flexible wobble stick with translational (150 mm stroke), rotational (360°), and 44° tilt motion (UHV Design, WS40-150-H) was attached to the side port. The end of the wobble stick was connected to a copper wire frame that was bent to make approximately a spoon shape and size. The wire frame was used to fix stainless steel wire mesh with 88% transparency consisting of 478 μm opening and 0.03 mm wire diameter (TWP Inc., Berkeley, CA; 050X050T0012). Solid sample particles of size between 0.5 and 2.0 mm were then placed onto the wire mesh. The wobble stick was carefully moved to levitate the sample at the levitation nodes and carefully retracted to avoid disturbance to the acoustic waves. These liquid and solid sample delivery system designs are somewhat similar to that independently developed by Brotton et al.[9,24] The reaction chamber was tested for leaks using a side port, as depicted in Figure 1. A three-way T-connector was used to connect the reaction chamber with a vacuum pump and a gas inlet line. Teflon tubing (0.25 in.) and Swagelok valve fitting deliver the desired gas to the chamber after chamber gas evacuation. For the evacuation of the chamber, the gas inlet valve is closed while the valve toward an air-cooled pumping station (Pfeiffer Vacuum, Germany, HiCube Eco) was opened. A flexible aluminum hose connects the chamber to the vacuum pumping station. A typical chamber base pressure of 10^{-6} torr was reached in 10 min with a 1500 rpm turbo pump speed. Pressures were monitored using a digital display single controller (K.J. Lesker, KJL354) with two different gauges: a convection gauge (K.J. Lesker, KJL275071) and an ionization gauge (K.J. Lesker, IG4YF). While the convection gauge monitored high-pressure range (10^{3} to 10^{-2} torr), the ionization gauge monitored low pressure (10^{-3} to 10^{-8} torr).

2.2. Raman Spectrometer System. A custom Raman spectrometer system was designed, assembled, and tested for *in situ* and online reaction monitoring. The schematic diagram of the major components of the system is shown in Figure 2. A 532 nm Nd:YAG laser (CrystaLaser, QL532-1W0) was guided into the chamber through a view port with 90% transmittance (K. J. Lesker, VPZL-275Q) using a high reflectance 45° broadband mirror (Thorlabs, BB1-E02) and a RazorEdge dichroic laser beam splitter (AVR Optics, LPD02-532RU), passing through a 500 mm diameter and 515 mm focal length plano-convex lens (CVI laser optics, PLCX-50.8-51.5-UV) before reaching the sample at the center of the reaction chamber with a 1 mm beam diameter. Upon striking the sample, the backscattered light is collected through the view port and filtered by the dichroic beam splitter, passing into a notch filter (Thorlabs, NF533-17) and focused via a plano-convex focusing lens (Thorlabs, LA4874) onto the slit (10 μm to 3 mm) of an Isoplane spectrograph (Princeton Instruments, IsoPlane 160). Note that the beam splitter was chosen carefully to allow maximum laser light reflectance (96.5% at 532 nm) while optimizing the transmittance (50.0% at 535 nm, and 97.4% at 538 nm) of Stokes Raman scattered photons. The beam splitter transmission was rated as T_{avg} > 93% between 538.9 and 824.8 nm. The notch filter was fixed at the 0° angle of incidence but can be used to change transmittance over a range of wavelengths by adjusting the angle of incidence. An air-cooled (−20 °C) front-illuminated charge-coupled device (CCD) camera with 1024 × 1024 horizontal and vertical pixels with a pixel size of 13 μm (Princeton Instruments, PI-MAX4:1024f) was mounted onto a side of the Isoplane spectrograph. The overall Raman system design is similar to

https://doi.org/10.1021/acsomega.1c00921
ACS Omega 2021, 6, 10447−10453

that reported by Bennett et al.[25] and Brotton and Kaiser.[4] In addition to photon collection optics, the major difference in our system from the above-mentioned systems lies in three available gratings that can be interchanged within seconds to achieve desired spectral resolution and range as well as smaller camera pixel size of 13 μm compared to 26 μm.

The Isoplane spectrograph and CCD camera were connected to a computer interface and controlled by LightField software (Princeton Instruments), which also allowed data recording and processing. Synchronization of the excitation laser, spectrograph, and CCD camera was done as follows. The spectrometer and CCD were controlled by LightField via the USB and GigE interface. A function generator (Quantum Composers, PG9514) outputs a TTL pulse via BNC connection that triggered the CCD camera at the desired repetition rate (typically 1 Hz to 1 kHz). The output from the camera circuit board then triggered the external input of the excitation laser. The output from the laser further triggered the spectrometer and camera with adjustable gated delay and width for scattered photon collection. A typical gate delay of 300 ns from laser excitation time and a gate width of 250 ns were used in the data described in this paper. The Isoplane spectrograph was equipped with a turret containing three different dispersion gratings of size 40 mm × 40 mm with 300, 600, and 1200 grooves/mm with 500 nm blaze wave length, which provides about 70% efficiency in the collection range. For 100 μm entrance slit and cyclohexane sample, the full width at half peak maximum were 38, 18, and 8 cm^{-1} for 300, 600, and 1200 grooves/mm gratings, respectively. The observable Raman shift range for these gratings was 5000, 2500, and 1000 cm^{-1}. The LightField software allowed selection of a particular grating and center wavelength within few seconds. The gating of the detector allowed filtration of background room light as well as an unwanted fluorescence signal from the sample. Such gating ability not only allows operation of the data collection at normal room light but also increases the Raman signal-to-noise ratio. Note that our system employs sample at a long distance from collection optics and spectrometer as opposed to commercial Raman system where sample-scattered photons are collected at a close distance to optimize the signal strength. One important parameter in spectrometer sensitivity and resolution was the entrance slit size. Figure 3 shows the effect of the slit size on peak intensity and peak resolution for various slit openings for 300 grooves/mm grating of cyclohexane. As evident from the graph, a doublet peak appears below 50 μm entrance slit allowing better resolution but at the expense of intensity.

2.3. Spectrometer Calibration and *In Situ* Reaction Monitoring. The Isoplane spectrograph provides the scan range of 0−1400 nm, wave length accuracy of 0.2 nm, and sub-pixel repeatability utilizing an AccuDrive grating scan system controlled by the LightField command. The dispersed light from the spectrograph was recorded by PI-MAX4 iCCD in its 1024 × 1024 pixels. The initial calibration and wavelength accuracy check of the camera pixels was performed by utilizing a neon lamp source in the visible range of electromagnetic spectrum by placing it outside the entrance slit of the Isoplane spectrograph. Spectra were recorded using neon emission lines for each of the three gratings using 650 nm center wavelength in the camera pixel. First, the bandwidths were examined for different slits of 10, 20, 30, 40, 50, and 100 μm size. Below 20 μm, the bandwidths did not change. Hence, we analyzed bandwidths and range of the spectrometer at a 20 μm slit

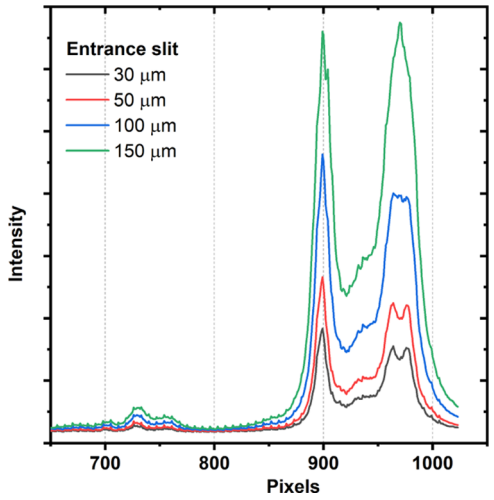

Figure 3. Effect of spectrograph light entrance slit size on peak intensity and resolution.

width by calibrating neon emission lines. Linear fits correlating camera pixel number to atomic emission wavelength were used. For 300 grooves/mm grating, the spectrometer range was 200 nm with a band full width at half-maximum (fwhm) of 1 nm (20 cm^{-1}). For 600 grooves/mm grating, the spectrometer range was 100 nm with a band fwhm of 0.52 nm (10 cm^{-1}). For 1200 grooves/mm grating, the spectrometer range was about 50 nm with a band fwhm of 0.19 nm (5 cm^{-1}). Hence, in our spectrometer, the best possible band fwhm is 5 cm^{-1}. For our fixed laser excitation at 532 nm, the center wave length of the detector was adjusted to a desired value to capture the Raman scattered photons. The current system utilizes optics to collect the Stokes shift but anti-Stokes shift can be recorded by adjusting the center wavelength within a few seconds utilizing the LightField control. Stokes shift range of 0−4500 cm^{-1} covers most of the vibrational region, which can be achieved in a current set up with 300 grooves/mm. The 600 grooves/mm grating provides better resolution and still can cover the desired range in most experiments. In the case of higher desired resolution, 1200 grooves/mm grating can be used to monitor the Raman peaks within a short range, but at least two different recordings are required to cover the long range due to its 1000 cm^{-1} range for one recording. Figure 4 shows the Raman shift calibration using cyclohexane for three different gratings mentioned above with typical photon collection times of 50−500 μs. The 50−500 μs collection time equals to 200 ns of gate width, 50 on-CCD collections, and 5−50 of such cycles. Dispersive slit images were recorded and converted to cross sections for graphing. Cross sections were generated by binning each CCD pixel column summing the intensities from each pixel column to produce a single data point for each pixel column. For each grating, a graph of spectroscopic peak maximum pixel number versus Raman shift was created, where the Raman shift values were taken from the NIST database.[26] While linear equation fittings yielded satisfactory results, quadratic fits to the data points gave best results with errors of ±5, ±2, and ±2 cm^{-1} for 300, 600, and 1200 grooves/mm gratings, respectively. The errors represent the standard deviation of Raman shift values from the NIST data. Data were taken at 100 μm slit width, which provided sufficient resolution to monitor the cyclohexane peaks even at lowest resolution grating. The peak at zero Raman shift arises due to

https://doi.org/10.1021/acsomega.1c00921
ACS Omega 2021, 6, 10447−10453

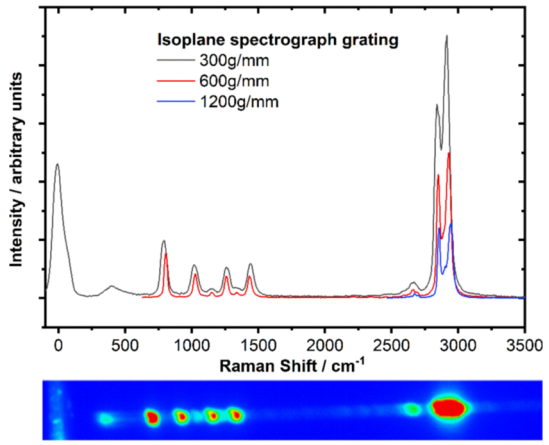

Figure 4. Cross sections of Raman signal recorded for cyclohexane with three different spectrograph gratings as indicated by differently colored graphs. The signal at zero Raman shift is due to the excitation laser. The actual image with 300 grooves/mm grating is shown at the bottom as a representative image.

scattered excitation laser light from multiple surfaces entering through the entrance slit. Using the cyclohexane fingerprint region bands, the peak fwhm values were determined to be 63, 56, 61, and 61 cm^{-1} for the four peaks recorded with 300 grooves/mm grating. For the 600 grooves/mm grating and same peaks, the fwhm values were 38, 35, 36, and 28 cm^{-1}, respectively. Such typical values of fwhm for a peak for different gratings were 60, 36, and 32 cm^{-1}, respectively, also illustrated by the 2930 cm^{-1} $-CH_2$ asymmetric stretch peak. Pelletier reported liquid cyclohexane bands with a bandwidth of about 10 cm^{-1} with a 3 s collection time and a 25 μm slit width utilizing a holoplex transmission grating.[27] Our bandwidths are larger than those reported by Pelletier due to the larger slit width but needed much shorter collection time as a consequence. Note that these fwhm values are typical for this calibration and can be optimized for higher resolution by changing collection focus at the entrance slit and the slit width. The 2930 and 2850 cm^{-1} bands arise due to a_{1g} $-CH_2$ asymmetric stretches. Assignments of these and complete vibrational bands of cyclohexane can be found elsewhere.[26,28]

2.4. Tunable Light Source for Photoreaction. A tunable monochromatic light source was interfaced via a view port to the reaction chamber as shown in Figure 1. The light source includes a 300 W/15 A ozone-free xenon arc lamp, lamp power supply and control, beam optics, and a Cornerstone 130 monochromator (Newport Corporation, TLS-300XU) with the output light range from 250 to 2400 nm. In the optimum output range of 300 −1800 nm and a slit size of 280 μm, a spectral resolution of 0.7 nm and a bandwidth of 3.7 nm can be achieved with a typical beam output size of 20 mm and 600 lines/mm diffraction grating. A bandwidth of 8 nm was obtained with a 600 μm slit size. The wavelength accuracy was typically 1 nm with 5% beam uniformity. The output optical power was about 0.1 mW and the irradiance was 0.2 mW/cm^2 for a 0.5 cm^2 beam area between 350 and 600 nm, with as much as 3 times higher power in the 800−1000 nm range. The output beam was aligned using vertical and horizontal adjustment knobs on the lamp housing door, rear reflector adjustment knobs on the lamp housing side panel, and focused to the center of the chamber using a lens inside the chamber. The beam size can be adjusted with extra focusing lenses, as necessary. The TLS-300XU system was connected to a control computer using an USB interface and TracQ, Oriel's instrument control, and data acquisition software. The TracQ software allowed quick library file load and control of output wavelength with an accuracy of about 1 nm.

To demonstrate the efficiency of the light source in chemical and physical transformations of a sample, experiments were performed by levitating a polystyrene sphere of diameter 0.99 mm (Cospheric, PSS-1.05) under room temperature and pressure conditions. Figure 5 shows the cross sections of

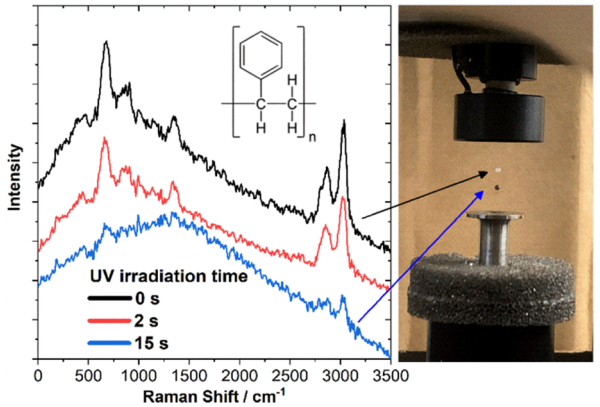

Figure 5. Raman spectra of a polystyrene sphere at different times (increasing irradiation time from top to bottom graphs) irradiated with 250 nm UV light (left panel). Near-total loss of structure was observed after 15 s irradiation. The physical transformation from white to black was observed due to UV irradiation as shown in the right panel.

dispersive slit images of polystyrene spheres at different UV irradiation times. Each trace is for a total of 25 μs of collection time. Three different traces of Raman signals at 0, 2, and 15 s of 250 nm photon irradiation times are shown from top to bottom graphs. The higher background counts at lower Raman shift values were due to fluorescent light resulting from polystyrene at lower wave lengths. These spectra contain at least three distinct regions with vibrational bands of polystyrene. Bands at lowest Raman shift represent $-CH_2$ rocking motion, at middle represent $-CH_2$ bending motion, and at higher Raman shift $-CH_2$ stretch and $-CH$ stretch of phenyl group.[29] Degradation of polymer structures, due to dehydrogenation reactions, became apparent after 2 s of irradiation time while complete loss of structures was observed after 15 s. Such transformation was also visible physically, with white to black color change before and after irradiation, as shown in the right panel of Figure 5.

Figure 6 shows the effect of photobleaching by 532 nm visible light on a freshly sliced potato sample. Even with optimized gating conditions of a detector, the Raman spectrum is dominated by fluorescence light from the sample, masking the Raman peaks as shown in the top trace in Figure 6. Up to 1 h of photobleaching by the tunable light source at two wavelengths, 450 and 532 nm did not change the spectrum significantly, likely due to insufficient number of photons. Spectra were then recorded for photobleaching utilizing a 532 nm laser with a 60 mW power at 2, 4, 10, 15, and 30 min of excitations. Significant change in the spectra were observed on first 2 min where the fluorescence reduced and two Raman peaks became clearly visible. To prevent the photobleaching

https://doi.org/10.1021/acsomega.1c00921
ACS Omega 2021, 6, 10447−10453

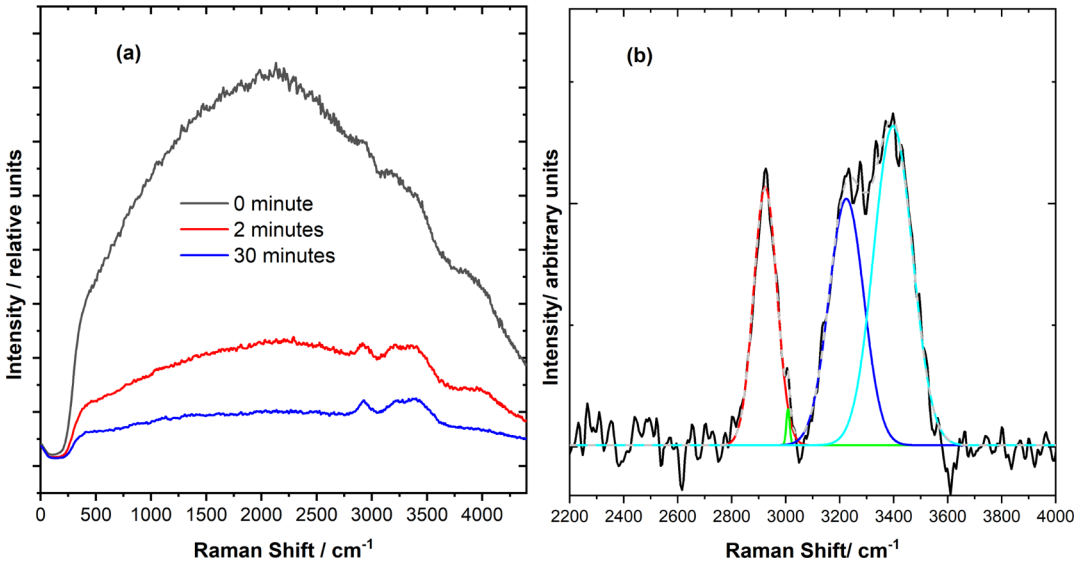

Figure 6. (a) Raman spectra of a freshly sliced potato as a function of 532 nm photon irradiation times. Photobleaching of the sample allows reduction in fluorescence background and enhanced Raman signatures. (b) Baseline-corrected and deconvoluted spectra for 30 min of irradiation time in the high-frequency region.

during recording of the spectra, very short excitation times (6 μs) were used. A small reduction in the background and an improvement in the spectra were observed after that, as shown in the 30 min spectra in Figure 6a. Two broad Raman bands near 2900 and 3400 cm^{-1} were attributed to C−H stretching and O−H stretching vibrations from carbohydrate and water since the typical carbohydrate and water contents in potatoes are 19 and 77%, respectively.[30] Figure 6b shows the baseline-corrected, deconvoluted spectra for 30 min irradiation in the high-frequency region. Amorphous starch has low-frequency bands in the fingerprint region but too weak to be detected in our setup. Gaussian fits to the data with an R^2 value of 0.982 were obtained. Experimental spectrum is shown in solid black curve while the cumulative overall fit is shown in dashed gray curve. The C−H stretching region can be fit with a major peak at 2923 cm^{-1} (red) and a minor peak at 3009 cm^{-1} (green). Similarly, the O−H stretching region can be fit with two peaks at 3224 cm^{-1} (blue) and 3398 cm^{-1} (cyan) with a relative magnitude of roughly 40:60%, respectively. These values match fairly well with previously reported spectra for potato.[31] These results demonstrate that the 532 nm laser can be used as an effective photobleaching source as well as Raman excitation source.

3. CONCLUSIONS

The design and fabrication of a process chamber with controlled gas pressure was presented. While a levitator was utilized to hold a liquid droplet or a solid particle sample inside the chamber, a tunable wavelength light source was used as a reaction perturbation source. The physical and chemical changes at the gas−surface interface were monitored by a custom-built Raman spectrometer system. Three different gratings can be interchanged within seconds for a desired spectroscopic range and resolution. The gating capability of the detector allows operation at room light and selective detection of Raman photons from fluorescence. The performance of the device is demonstrated by degradation of polystyrene by UV light and photobleaching of potato by visible light. This versatile platform for *in situ* reaction monitoring can be applied in varieties of fields, such as in astrochemistry-simulating heterogeneous atmospheric chemical reactions, in molecular biology in detection and monitoring of organic compounds, and in materials science to visualize surface-catalyzed reactions. The *in situ* spectroscopic monitoring over time also allows investigation of kinetics of chemical reactions.

AUTHOR INFORMATION

Corresponding Author

Beni B. Dangi − *Department of Chemistry, Florida Agricultural and Mechanical University, Tallahassee, Florida 32307, United States;* orcid.org/0000-0002-1866-8725; Email: beni.dangi@famu.edu

Author

Daniel J. Dickerson − *Department of Chemistry, Florida Agricultural and Mechanical University, Tallahassee, Florida 32307, United States*

Complete contact information is available at: https://pubs.acs.org/10.1021/acsomega.1c00921

Notes

The authors declare no competing financial interest.

ACKNOWLEDGMENTS

This project was supported by NASA through the NASA Florida Space Grant Consortium (project #006981). The authors also acknowledge Dr. Charlemagne Akpovo for helpful discussions in selection of optical components of the Raman system.

REFERENCES

(1) Lierke, E. G. Acoustic levitation - A comprehensive survey of principles and applications. *Acustica* **1996**, *82*, 220−237.
(2) Zang, D.; Yu, Y.; Chen, Z.; Li, X.; Wu, H.; Geng, X. Acoustic levitation of liquid drops: Dynamics, manipulation and phase transitions. *Adv. Colloid Interface* **2017**, *243*, 77−85.
(3) Bänsch, E. G.; Michael, G. Numerical study of droplet evaporation in an acoustic levitator. *Phys. Fluids* **2018**, *30*, 037103.

(4) Brotton, S. J.; Kaiser, R. I. Novel high-temperature and pressure-compatible ultrasonic levitator apparatus coupled to Raman and Fourier transform infrared spectrometers. *Rev. Sci. Instrum.* **2013**, *84*, 055114.
(5) Dangi, B. B.; Kim, Y. S.; Krasnokutski, S. A.; Kaiser, R. I.; Bauschlicher, C. W., Jr. Toward the Formation of Carbonaceous Refractory Matter in High Temperature Hydrocarbon-Rich Atmospheres of Exoplanets Upon Micrometeoroid Impact. *Astrophys. J.* **2015**, *805*, 76.
(6) Cao, H.-L.; Yin, D.-C.; Guo, Y.-Z.; Ma, X.-L.; He, J.; Guo, W.-H.; Xie, X.-Z.; Zhou, B.-R. Rapid crystallization from acoustically levitated droplets. *J. Acoust. Soc. Am.* **2012**, *131*, 3164−3172.
(7) Cristiglio, V.; Grillo, I.; Fomina, M.; Wien, F.; Shalaev, E.; Novikov, A.; Brassamin, S.; Réfrégiers, M.; Pérez, J.; Hennet, L. Combination of acoustic levitation with small angle scattering techniques and synchrotron radiation circular dichroism. Application to the study of protein solutions. *Biochim. Biophys. Acta Gen. Subj.* **2017**, *1861*, 3693−3699.
(8) Combe, N. A.; Donaldson, D. J. Water Evaporation from Acoustically Levitated Aqueous Solution Droplets. *J. Phys. Chem. A* **2017**, *121*, 7197−7204.
(9) Brotton, S. J.; Kaiser, R. I. Controlled Chemistry via Contactless Manipulation and Merging of Droplets in an Acoustic Levitator. *Anal. Chem.* **2020**, *92*, 8371−8377.
(10) Bjelobrk, N.; Nabavi, M.; Poulikakos, D. Acoustic levitator for contactless motion and merging of large droplets in air. *J. Appl. Phys.* **2012**, *112*, 053510.
(11) Tsujino, S.; Shinoda, A.; Tomizaki, T. On-demand droplet loading of ultrasonic acoustic levitator and its application for protein crystallography experiments. *Appl. Phys. Lett.* **2019**, *114*, 213702.
(12) Mason, N. J.; Drage, E. A.; Webb, S. M.; Dawes, A.; McPheat, R.; Hayes, G. The spectroscopy and chemical dynamics of microparticles explored using an ultrasonic trap. *Faraday Discuss.* **2008**, *137*, 367−376.
(13) Li, L.; Gu, N.; Dong, H.; Li, B.; G, K. T. V. Analysis of the effects of acoustic levitation to simulate the microgravity environment on the development of early zebrafish embryos. *RSC Adv.* **2020**, *10*, 44593−44600.
(14) Hasegawa, K.; Watanabe, A.; Abe, Y. Acoustic Manipulation of Droplets under Reduced Gravity. *Sci. Rep.* **2019**, *9*, 16603.
(15) He, C.; Hörst, S. M.; Lewis, N. K.; Yu, X.; Moses, J. I.; Kempton, E. M.-R.; Marley, M. S.; McGuiggan, P.; Morley, C. V.; Valenti, J. A.; Vuitton, V. Photochemical Haze Formation in the Atmospheres of Super-Earths and Mini-Neptunes. *Astron. J.* **2018**, *156*, 38.
(16) Dangi, B. B.; Kattel, S. Growth of carbonaceous material on silicon surface: Case study of 1,3-butadiene molecule. *Chem. Phys. Lett.* **2020**, *745*, 137248.
(17) Maruyama, Y.; Hasegawa, K. Evaporation and drying kinetics of water-NaCl droplets via acoustic levitation. *RSC Adv.* **2020**, *10*, 1870−1877.
(18) Yu, Y.; Qu, S. H.; Zang, D. Y.; Wang, L. D.; Wu, H. J. Fast Synthesis of Pt Nanocrystals and Pt/Microporous La2O3 Materials Using Acoustic Levitation. *Nanoscale Res. Lett.* **2018**, *13*, 50.
(19) Habel, C.; Maiz, J.; Olmedo-Martinez, J. L.; Lopez, J. V.; Breu, J.; Muller, A. J. Competition between nucleation and confinement in the crystallization of poly(ethylene glycol)/large aspect ratio hectorite nanocomposites. *Polymer* **2020**, *202*, 122734.
(20) Meldrum, F. C.; O'Shaughnessy, C. Crystallization in Confinement. *Adv. Mater.* **2020**, *32*, 2001068.
(21) Dangi, B. B.; Dixon, J. M.; Alexander, S.; Noel, E. An acoustic levitator for single droplet evaporation kinetics. *Res. J. Chem. Sci.* **2020**, *10*, 32−37.
(22) Ehrenreich, D.; des Etangs, A. L.; Delfosse, X. HST/STIS Lyman-alpha observations of the quiet M dwarf GJ 436 Predictions for the exospheric transit signature of the hot Neptune GJ 436b. *Astron. Astrophys.* **2011**, *529*, A80.
(23) Dos Santos, L. A.; Bourrier, V.; Ehrenreich, D.; Kameda, S. Observability of hydrogen-rich exospheres in Earth-like exoplanets. *Astron. Astrophys.* **2019**, *622*, A46.
(24) Brotton, S. J.; Malek, M. J.; Anderson, S. L.; Kaiser, R. I. Effects of acetonitrile-assisted ball-milled aluminum nanoparticles on the ignition of acoustically levitated exo-tetrahydrodicyclopentadiene (JP-10) droplets. *Chem. Phys. Lett.* **2020**, *754*, 137679.
(25) Bennett, C. J.; Brotton, S. J.; Jones, B. M.; Misra, A. K.; Sharma, S. K.; Kaiser, R. I. High-Sensitivity Raman Spectrometer To Study Pristine and Irradiated Interstellar Ice Analogs. *Anal. Chem.* **2013**, *85*, 5659−5665.
(26) Shimanouchi, T. *Tables of Molecular Vibrational Frequencies Consolidated Volume I*; US Government Printing Office, 1972.
(27) Pelletier, M. J. Effects of temperature on cyclohexane Raman bands. *Appl. Spectrosc.* **1999**, *53*, 1087−1096.
(28) Miller, F. A.; Golob, H. R. The infrared and Raman spectra of cyclohexane and cyclohexane-d12. *Spectrochim. Acta* **1964**, *20*, 1517−1530.
(29) Palm, A. Raman Spectrum of Polystyrene. *J. Phys. Chem.* **1951**, *55*, 1320−1324.
(30) Pedreschi, F.; Cocio, C.; Moyano, P.; Troncoso, E. Oil distribution in potato slices during frying. *J. Food Eng.* **2008**, *87*, 200−212.
(31) Sun, D.-W.; Li, D.; Zhu, Z. Method for testing water content and water distribution of cellular levels in fruit and vegetable tissues on basis of raman spectrum. WO2020252999A1, 2020. CODEN:-PIXXD2.

https://doi.org/10.1021/acsomega.1c00921
ACS Omega 2021, 6, 10447−10453